

Phononic dissipation during “hot” adatom motion: A QM/Me study of O₂ dissociation at Pd surfaces

Cite as: J. Chem. Phys. **146**, 014702 (2017); <https://doi.org/10.1063/1.4973244>

Submitted: 13 September 2016 • Accepted: 13 December 2016 • Published Online: 03 January 2017

 Vanessa J. Bukas and  Karsten Reuter



View Online



Export Citation



CrossMark

ARTICLES YOU MAY BE INTERESTED IN

[Fingerprints of energy dissipation for exothermic surface chemical reactions: O₂ on Pd\(100\)](#)

The Journal of Chemical Physics **143**, 034705 (2015); <https://doi.org/10.1063/1.4926989>

[Dynamics in reactions on metal surfaces: A theoretical perspective](#)

The Journal of Chemical Physics **150**, 180901 (2019); <https://doi.org/10.1063/1.5096869>

[Automatically growing global reactive neural network potential energy surfaces: A trajectory-free active learning strategy](#)

The Journal of Chemical Physics **152**, 154104 (2020); <https://doi.org/10.1063/5.0004944>

The Journal of Chemical Physics **Special Topics** Open for Submissions [Learn More](#)

Phononic dissipation during “hot” adatom motion: A QM/Me study of O₂ dissociation at Pd surfaces

Vanessa J. Bukas^{a)} and Karsten Reuter

Chair for Theoretical Chemistry and Catalysis Research Center, Technische Universität München, Lichtenbergstr. 4, D-85747 Garching, Germany

(Received 13 September 2016; accepted 13 December 2016; published online 3 January 2017)

We augment *ab initio* molecular dynamics simulations with a quantitative account of phononic dissipation to study the non-equilibrium aftermath of the exothermic oxygen dissociation at low-index (111), (100), and (110) Pd surfaces. Comparing the hyperthermal diffusion arising from a non-instantaneous dissipation of the released chemical energy, we find a striking difference in the resulting “hot” adatom lifetime that is not overall reflected in experimentally recorded product end distances. We rationalize this finding through a detailed mode-specific phonon analysis and identify the dominant dissipation channels as qualitatively different groups of localized surface modes that ultimately lead to intrinsically different rates of dissipation to the Pd bulk. The thus obtained first-principles perspective on non-equilibrium adsorbate-phonon dynamics thereby underscores the sensitive dependence on details of the phononic fine structure, while questioning prevalent assumptions about energy sinks made in commonly used model bath Hamiltonians. *Published by AIP Publishing.* [<http://dx.doi.org/10.1063/1.4973244>]

I. INTRODUCTION

Surface diffusion is a vital step in a number of important surface dynamical processes such as epitaxial growth, the self-assembly of surface nanostructures, or catalytically relevant chemical reactions. The prevalent notion of thermal diffusion presupposes the adsorbate’s continuous equilibration with the surface and correspondingly predicts a temperature dependence dictated by the substrate temperature. This is contrasted by the concept of hyperthermal transient mobility, which results from the intrinsic exothermicity of an immediately preceding elementary step like (dissociative) adsorption. The hyperthermal diffusion is then governed by the delayed energy dissipation to the underlying substrate rather than the substrate’s overall temperature. A corresponding transient mobility has been proposed recurrently and attracts increasing attention for instance in view of its ability to generate “hot” precursors for subsequent reaction steps.¹ Ensuing, for example, the (exothermic) dissociative oxygen adsorption, resulting hot O adatoms have been suggested to promote oxide nucleation at low temperatures² while also offering promises for opening up low-energy pathways in oxidation catalysis.³

Despite this suspected importance, it has hitherto proven rather challenging to really grasp such hyperthermal diffusion processes even in the idealized regime of single-crystal surfaces and ultra-high vacuum (UHV). Experiments providing the required atomic spatial resolution are unable to explicitly access the picosecond dynamical motion. Instead, the hyperthermal motion is at best indirectly inferred in scanning tunneling microscopy (STM) studies performed at temperatures that are sufficiently low to suppress thermal diffusion. Such

studies focused heavily on the dissociative and highly exothermic adsorption of O₂ at transition metal surfaces.^{4–9} An ensuing transient mobility is there derived from recorded larger separation distances of adatom pairs—an indirect procedure that has caused quite some controversy.¹⁰

Predictive-quality theoretical work would provide the necessary spatial and temporal resolution, yet has struggled with the necessity to both provide a reliable account of the quantum-mechanical (QM) surface chemical interactions and the heat dissipation into the phononic degrees of freedom. Straightforward *ab initio* molecular dynamics (AIMD) simulations in computationally tractable supercell geometries suffer from unphysical phonon reflections at the periodic boundaries and an inadequate description of the phononic band structure. Alternatively pursued Langevin-type approaches remove the phonon reflections in finite-size supercells by relying on bath Hamiltonians to describe the phononic degrees of freedom, cf., for example, Refs. 11–13. The practical bottleneck here is the assumptions that have to be made with respect to the bath Hamiltonian. With very little generally known about adsorbate-surface or surface-bath coupling constants, rather crude descriptions represent the state of the art. Based mainly on energetic considerations, low-frequency Rayleigh modes are, for instance, generally assumed to be predominantly excited upon first impact with the surface. Some justification for this conjecture has in fact been provided by early studies of light atomic or molecular species scattering off noble metals (cf., for example, see Ref. 14 and references therein), while instances have also been reported to put it into question.²⁴ The validity extent of this assumption thus overall remains to its larger extent unknown. On the other hand, there is vice versa the question of how well these microscopic details need to be described from a modeling perspective in

^{a)}Electronic mail: vanessa.bukas@ch.tum.de

order to arrive at a reliable description of the actual adsorbate dynamics.

In this situation, the recent advent of the QM/molecular modeling (MM) embedding approach for metals (originally coined, and hence referred to, as “QM/Me”) allowed for a big step forward.¹⁵ Within a multi-scale modeling philosophy, this embedding scheme complements a density-functional theory (DFT) based treatment of the immediate reaction zone around the adsorbate impingement site with a quantitative treatment of phononic dissipation into an extended substrate described at the molecular modeling (MM) level. In a first comparative study applying this QM/Me scheme to different metal facets we compared the hot adatom diffusion ensuing O₂ dissociation over Pd(100) and Pd(111).¹⁶ This revealed the experimentally accessible product end distances as a rather misleading measure for the lifetime of the hyperthermal state. The latter was found to be particularly long at Pd(111), where a random-walk type diffusion leads only to small net displacements. In contrast, the symmetry of the more “open” Pd(100) surface allows for channel-type diffusion and concomitant longer net displacements—yet at a rather short lifetime.

This already demonstrates a complex dependence on microscopic details of the dissipative dynamics. Here, we now directly investigate the role of substrate symmetry by providing a detailed mode-specific phonon analysis to compare the equilibration ensuing O₂ dissociation at all three low-index (111), (100), and (110) Pd facets. Despite the similarly high exothermicity of the dissociative reactions and comparable barriers for atomic diffusion, we find a striking difference in the degree of the resulting hyperthermal mobility, i.e., the O adatoms remain “hot” for shorter or longer periods of time on each of the substrates. We rationalize this finding by identifying the dominant dissipation channels as qualitatively different surface modes that do not necessarily involve the Rayleigh modes at the lower energy end of the phononic spectra. This ultimately leads to intrinsically different rates of dissipation from the three surfaces to the Pd bulk, as verified by quantifying the phononic energy uptake directly from the QM/Me-AIMD trajectories. We thus overall underscore the importance of modeling the “right” surface excitations, while offering a first-principles perspective on the phonon parameters that enter prevalent heat bath models.

II. METHODS

A. QM/Me: An embedding approach for metals

QM/Me is an embedding scheme specifically designed to treat dynamical processes at metal surfaces.¹⁵ Its originality, in comparison to QM/MM embedding as routinely employed in the modeling of biomolecules or band-gap materials,^{17–19} lies in avoiding the use of finite QM clusters. The embedded QM region is instead calculated using periodic boundary condition (PBC) supercells, as is required to fully capture the delocalized metallic band structure and its crucial importance to adsorption. The embedding into the MM region is then achieved by separating the chemical and elastic contributions in the QM interaction potential, which leads to the following embedding ansatz for an atom at position \mathcal{R} :

$$V^{\text{QM/Me}}(\mathcal{R}) = V^{\text{Me}}(\mathcal{R}_{\text{bath}}) + \underbrace{\left[E^{\text{QM}}(\mathcal{R}_{\text{slab}} \cup \mathcal{R}_{\text{ads}}) - E^{\text{QM}}(\mathcal{R}_{\text{slab}}) \right]}_{V^{\Delta\text{QM}}(\mathcal{R}_{\text{slab}} \cup \mathcal{R}_{\text{ads}})}, \quad (1)$$

where the coordinate sets $\mathcal{R}_{\text{bath}}$, $\mathcal{R}_{\text{slab}}$, and \mathcal{R}_{ads} correspond to all metal atoms in the MM simulation cell, to the metal atoms in the embedded QM supercell, and the adsorbate atoms, respectively.

Equation (1) defines $V^{\Delta\text{QM}}$ as the specific chemical adsorbate-substrate and adsorbate-adsorbate interactions. It is obtained in practice from two successive DFT calculations within identical periodic supercells: The first includes the adsorbate atoms and the second excludes them, while in both cases the positions of the substrate atoms ($\mathcal{R}_{\text{slab}}$) remain unchanged. Forming the difference of these calculations thus cancels contributions of elastic interactions in the metal substrate and leaves only the adsorbate-induced chemical interactions. The latter are sufficiently short-ranged to be well contained within the finite extent of computationally tractable supercells. Even though calculated within PBCs, $V^{\Delta\text{QM}}$ extends thus only over a finite region. V^{Me} then provides the missing elastic contributions from substrate-substrate interactions due to lattice deformations that occur with the progressing chemical reaction. They are accurately described by many-body classical interatomic potentials and the numerical efficiency of the latter allows to explicitly model them in an extended MM region. Several tens of thousand bath atoms can thus easily be included without the evaluation of V^{Me} becoming a computational bottleneck and without the simulation being affected by the lateral PBCs which we impose on the MM region for the sake of convenience.

“Embedding” $V^{\Delta\text{QM}}$ in V^{Me} through Eq. (1) thus complements first-principles based dynamical simulations of chemical reactions at metal surfaces with an explicit account of the energy dissipation into an atomically resolved heat bath. It is exactly this atomic resolution that lays the foundations for the phonon analysis described in Section II B and the thereby derived important information on the microscopic details of energy dissipation.

B. Phonon projection scheme

In the following we describe a rigorous projection scheme used to quantitatively assess phononic excitations in a mode-specific manner by using information that can be directly extracted from AIMD simulations. As already indicated, such an analysis is only made possible here by explicitly considering the atomistic details in the extended MM region and thus incorporating a realistic description of the phononic fine structure into the QM/Me Hamiltonian, cf. Eq. (1). A challenge remains, however, in making contact with the phonon dispersion relation in order to identify the nature of excited modes through their actual wave vector, while in the meantime circumventing the computationally formidable task of diagonalizing the dynamical matrix of an MM region that contains in excess of hundred thousand atoms.

We achieve this on the basis of a projection methodology that allows to represent the complex atomic displacement

pattern of the atoms in the large MM region as a superposition of the normal mode displacement eigenvectors of a laterally periodic surface primitive cell. Phonons realized in different branches at the $\bar{\Gamma}$ -point in the small Brillouin zone of the supercell are thus effectively back-folded into the (larger) Brillouin zone corresponding to the chosen surface primitive cell. The target phonon mode expansion coefficients then depend on time only through the real-space displacement field, which can be straightforwardly obtained at any time step of an MD trajectory. The projection scheme is thus rendered suitable for instantaneous application without the need for an averaging over time. This already offers a prodigious advantage over methods that rely on time autocorrelation functions to arrive at occupied phonon densities, in particular within first-principles based approaches for which a quantitative phonon analysis has thus far remained impractical or even impossible (cf., for example, Refs. 20–22).

The rigorous formulation of the phonon projection scheme was originally laid out by McGaughey and Kaviani for the monatomic ($N_{\text{cell}} = 1$) bulk primitive cell of Lennard-Jones model crystals.²³ For the present application on a two-dimensional slab that extends over a sufficient number of surface layers (N_{layers}) this has been appropriately extended to a polyatomic primitive cell, a detailed derivation of which may be found in Ref. 24. This cell specifically contains a single atom per layer for the low-index fcc surfaces investigated here ($N_{\text{cell}} = N_{\text{layers}}$), while an arbitrarily large supercell can then be constructed by ($N_1 \times N_2$) repetitions in the lateral periodic directions.

The starting point is then the atomic displacement field of the MM supercell containing $N_{\text{supercell}}$ ($\equiv N_1 \times N_2 \times N_{\text{layers}}$) atoms. This displacement field is described in the $3N_{\text{supercell}}$ -dimensional vector $\mathbf{U}^{\text{MD}}(t)$ that denotes the Cartesian displacements with respect to the equilibrium positions \mathbf{R}^0 at a given time t during the MD simulation. The vector is defined on the real-space lattice grid (\mathbf{L}_n) of the atomic positions and can be transformed onto the corresponding reciprocal grid (\mathbf{q}_n) of exact phonon wave vectors by means of a discrete two-dimensional spatial Fourier transform,

$$U_{i\alpha}^{\text{MD}}(\mathbf{L}_n; t) = \frac{1}{\sqrt{N_1 N_2}} \frac{1}{\sqrt{M_{\bar{l}}}} \times \sum_{\mathbf{q}_{n'}}^{\text{grid}} \left(\sum_{b'=1}^{3N_{\text{layers}}} C(\mathbf{q}_{n'}, b'; t) \hat{u}_{i\alpha}(\mathbf{q}_{n'}, b') \right) e^{i\mathbf{q}_{n'} \cdot \mathbf{L}_n}. \quad (2)$$

The transformation is performed component-wise with Cartesian vector coordinates $\alpha = (x, y, z)$ and for every atom in the supercell. The latter are indexed by a number \bar{l} in the primitive cell (denoting the specific surface layer) and a two-dimensional lattice vector \mathbf{L} leading to the desired periodic image (n) in the lateral directions. At every point $\mathbf{q}_{n'}$ the phonon mode expansion coefficients $C(\mathbf{q}_{n'}, b'; t)$, which are the key quantities of interest here, are represented in the orthonormalized basis of generally complex-valued displacement eigenvectors $\{\hat{u}_{i\alpha}(\mathbf{q}_{n'}, b')\}_{b'} \subset \mathbb{C}^{3N_{\text{layers}}}$, where b' is the phonon band index. Finally, masses ($M_{\bar{l}}$) are separated out of the latter which are therewith given in mass-weighted coordinates as is the common convention in lattice dynamics.

As already indicated above, \mathbf{q} -points of the reciprocal-space grid are chosen such that the two-dimensional periodicity of the phonons is commensurate with the chosen supercell and hence described exactly. Making use of the orthonormality relations for both the discrete Fourier transform and the displacement eigenvectors greatly simplifies the task of obtaining the target $C(\mathbf{q}_n, b; t)$ from Eq. (2) and leads to the following ansatz:

$$C(\mathbf{q}_n, b; t) = \frac{1}{\sqrt{N_1 N_2}} \sum_n^{N_1 \times N_2} \sum_{\bar{l}}^{N_{\text{layers}}} \sqrt{M_{\bar{l}}} [\hat{u}_{\bar{l}}(\mathbf{q}_n, b)]^* \cdot U_{n\bar{l}}^{\text{MD}}(t) e^{-i\mathbf{q}_n \cdot (\mathbf{R}_{n\bar{l}}^0 - \mathbf{R}_{\bar{l}}^0)}, \quad (3)$$

where the double-index $n\bar{l}$ iterates over all $N_{\text{supercell}}$ atoms in the MM supercell.

Following the same decomposition of Eq. (2) and the ensuing formalism also for the velocity field $\dot{\mathbf{R}}^{\text{MD}}(t)$ yields corresponding velocity expansion coefficients $\dot{C}(\mathbf{q}_n, b; t)$. Under the harmonic approximation, the total energy of a single phonon mode can then be expressed as

$$\varepsilon^{\text{ph}}(\mathbf{q}_n, b; t) = \varepsilon_{\text{kin}}^{\text{ph}}(\mathbf{q}_n, b; t) + \varepsilon_{\text{pot}}^{\text{ph}}(\mathbf{q}_n, b; t) = \frac{1}{2} |\dot{C}(\mathbf{q}_n, b; t)|^2 + \frac{1}{2} \omega^2(\mathbf{q}_n, b) |C(\mathbf{q}_n, b; t)|^2, \quad (4)$$

where the two terms correspond to the kinetic and (harmonic) potential energy of the corresponding mode with frequency ω . To the extent that the harmonic approximation holds, Eq. (4) thus forms the foundation for quantifying the total phononic energy uptake,

$$E_{\text{tot}}^{\text{ph}}(t) = \sum_{\mathbf{q}_n}^{\text{grid}} \sum_{b=1}^{3N_{\text{layers}}} \varepsilon^{\text{ph}}(\mathbf{q}_n, b; t), \quad (5)$$

while the provided mode selectivity allows to also focus on certain groups of modes and assess their role during the dissociation dynamics.

C. Computational and technical details

The oxygen-Pd interaction energetics are obtained by DFT calculations within the generalized gradient approximation and using the exchange correlation (xc) functional due to Perdew, Burke, and Ernzerhof (PBE).²⁵ The approximate account of electronic xc in the semi-local PBE functional is known to lead to spurious ferromagnetic ordering in bulk palladium.²⁶ To suppress this, we assume perfect quenching of the O₂ spin-triplet state close to the metal surface²⁷ and conduct all calculations in a non-spin polarized manner. Electronic states are described with an all-electron basis set as implemented within the FHI-aims code.²⁸ Specifically, the “tier2” basis set with the internal default `tight` settings for the numerical integrations is employed in the description of O atoms and Pd atoms belonging to the topmost surface layer. “Tier1” and `light` settings are chosen for all remaining Pd atoms. For the optimized O adsorption energies at all three considered Pd surfaces, this setup was found to significantly reduce the computational effort at an insignificant additional uncertainty <10 meV as compared to calculations performed at full “tier2”/tight level.

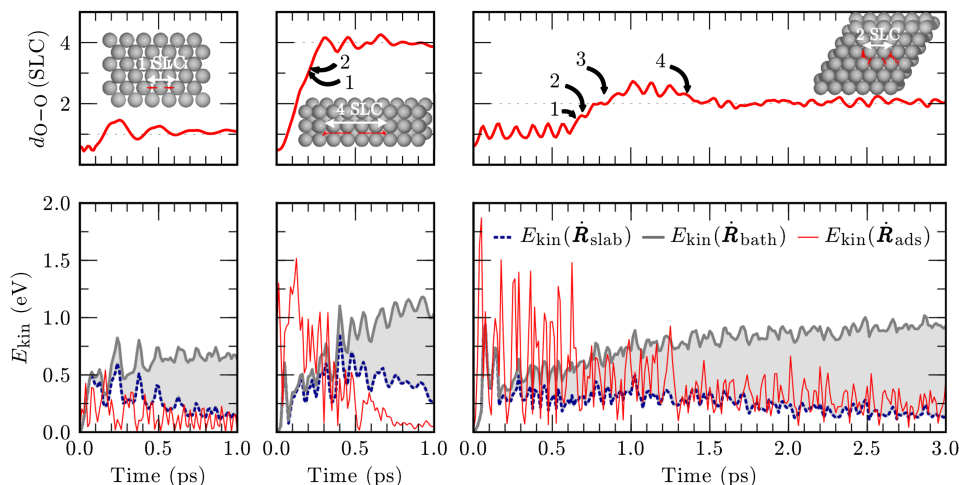


FIG. 1. Dynamical information extracted from representative QM/Me-AIMD trajectories for O_2 dissociating at Pd(110) (left), Pd(100) (middle), and Pd(111) (right). Top panels: Separation distance of the oxygen adatoms in units of the surface lattice constant (SLC, $\sim 2.8 \text{ \AA}$). Hyperthermal adatom hops are numbered and schematically represented in a top-view of the DFT-described reaction zones in the figure insets. Lower panels: Kinetic energy of the Pd atoms contained in the QM embedding cell $E_{\text{kin}}(\vec{R}_{\text{slab}})$ (dashed blue line), of all (125 000) Pd atoms in the heat bath $E_{\text{kin}}(\vec{R}_{\text{bath}})$ (thick gray line), and of the adsorbates $E_{\text{kin}}(\vec{R}_{\text{ads}})$ (thin red line). The area between the last two curves (shaded in gray) is correspondingly a measure of the heat dissipated outside of the QM reaction zone.

The effective separation of short-ranged chemical and long-ranged elastic interactions, crucially relied upon by QM/Me, holds only upon vanishing force differences $F^{\Delta\text{QM}}$ for Pd atoms at the boundaries of the embedded QM supercell and their larger distance from the adsorbate(s). Careful checks were thus performed to ensure that such force components on most distant atoms have decayed to $\leq 10^{-2} \text{ eV/\AA}^2$ in order to minimize boundary effects for the embedding cells employed in this work. These consist of three layer slabs which are (6×3) , (9×3) , and (6×6) multiples of the Pd(110), Pd(100), and Pd(111) surface unit cells, respectively. These QM supercells are illustrated in the insets of Fig. 1 and each features a vacuum region of 30 \AA . Calculations are performed using $(2 \times 4 \times 1)$, $(2 \times 4 \times 1)$, and $(2 \times 2 \times 1)$ Monkhorst-Pack grids²⁹ for k-point sampling of the O_2 -Pd(110), O_2 -Pd(100), and O_2 -Pd(111) systems, respectively. Using these computational settings consistently for both DFT calculations required at each time step (here, of a 2.5 fs length) during a QM/Me-based MD simulation ensures a numerically well-defined construction

of $F^{\Delta\text{QM}}(\vec{R}_{\text{slab}})$ with negligible embedding-induced errors, as also verified by the high-quality energy conservation ($< 0.5 \text{ meV}$ per atom) obtained for the investigated trajectories.

A cubic $(50 \times 50 \times 50)$ MM region, incorporating a total of 125 000 Pd atoms, is used to describe the long-range phonon propagation in all investigated Pd substrates. Such system sizes are still very much affordable within a classical treatment and ensure that phonon propagation has not yet reached the boundaries of the employed simulation boxes even for the longer trajectories (3 ps) considered in this work. The bath energetics are evaluated using the LAMMPS³⁰ package and at the level of a modified embedded atom method (MEAM) as originally developed by Baskes.³¹ For the Pd(100) and Pd(111) slabs we specifically employ the MEAM reparameterization used in the more recent work of Meyer and Reuter¹⁵ which was found to better reproduce first-principles based relaxation effects³² at these two surfaces. As already indicated, QM/Me forces are evaluated independently on the DFT, MM levels of theory and atomic positions are communicated between the two at each

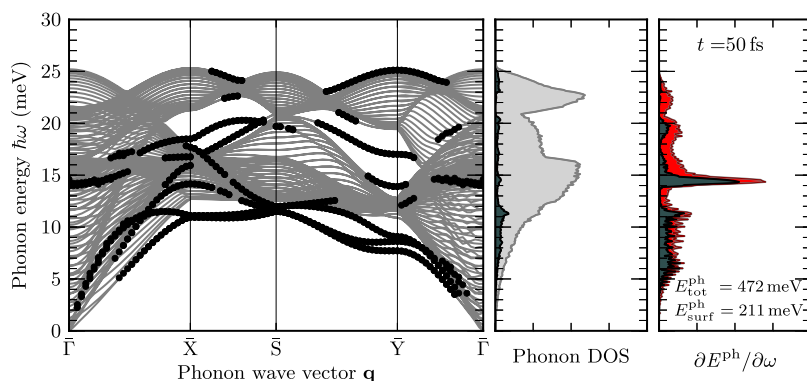
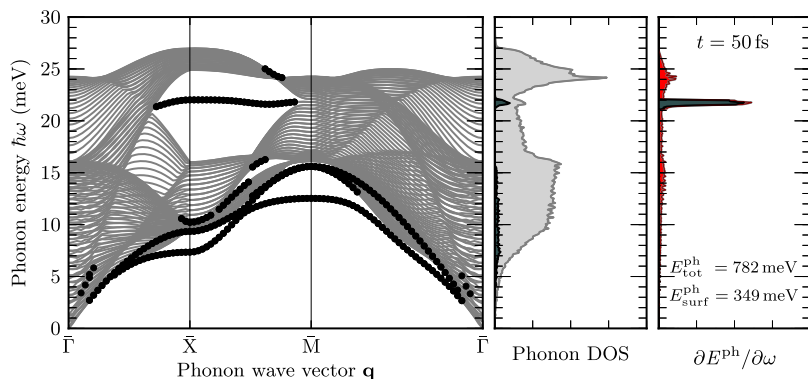


FIG. 2. Rightmost panel: Energy resolved phonon excitation spectrum calculated at $t = 50 \text{ fs}$ along the QM/Me-AIMD trajectory of O_2 dissociating at Pd(110) as described in the main text. The total amount of energy ($E_{\text{tot}}^{\text{ph}}$) along with the fraction assigned to surface modes ($E_{\text{surf}}^{\text{ph}}$) are noted and correspond to the areas shaded red and black, respectively. Middle and leftmost panels: The corresponding equilibrium bulk Pd phonon density of states (DOS) and phonon dispersion along the boundaries of the irreducible wedge are shown for reference. In all cases modes are classified as surface phonons if their displacement eigenvector is localized to $\geq 20\%$ in the outermost two slab layers and their contributions are indicated by black markers/thick lines.

FIG. 3. Same as Fig. 2 but for O₂ dissociating at Pd(100).

MD time step. The latter are automatically re-scaled here through the use of fractional coordinates in order to overcome the limitation imposed by any residual lattice mismatches between the MEAM and our PBE-DFT description of the Pd substrate. We note that qualitatively similar results are obtained in the context of the adsorbate equilibration dynamics for all investigated systems when employing either the original or reparameterized version of the MEAM potential.

Classical MD simulations are performed at a zero initial temperature within the NVE ensemble and according to the QM/Me embedding scheme. We loosely interface the calculations performed independently on the DFT and MEAM levels through the Atomic Simulation Environment (ASE).³³ Extending on the latter, a simple “master” script is responsible for the following: (i) properly communicating the coordinate and force sets during each time step of the MD simulation, (ii) collecting the ingredients needed to apply the embedding ansatz of Eq. (1), (iii) propagating the system in time via the Velocity Verlet algorithm, and (iv) book keeping the large input/output files.

Static stand-alone DFT calculations are performed based on the FHI-aims setup described above but employing five-layer (3 × 3) (or (4 × 4)) surface slabs with (4 × 4 × 1) (or (3 × 3 × 1)) Monkhorst-Pack grids for k-point sampling. Relaxations are conducted using the Broyden-Fletcher-Goldfarb-Shanno (BFGS) algorithm and a convergence criterion of $F_{\max} \leq 10^{-2}$ eV/Å. Vibrational modes of adsorbed oxygen atoms are obtained within the harmonic approximation by diagonalizing a finite difference approximation of the Hessian matrix as implemented within ASE. The forces are calculated for six displacements from the equilibrium state per oxygen atom: $\pm\delta$ for each Cartesian coordinate where δ is

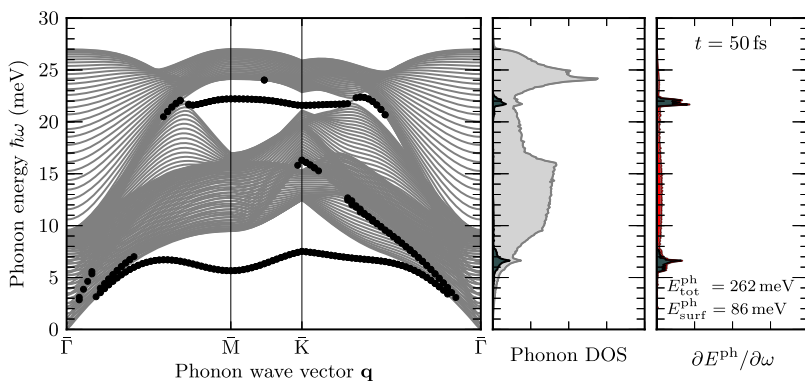
set to 10^{-2} Å. Finally, transition state (TS) searches are conducted with the ASE-implemented climbing image version of the Nudged Elastic Band (NEB) method,³⁴ while typically constraining all but the topmost one or two Pd surface layers for reasons of computational efficiency.

Phonon modes are calculated using the finite displacement method, based on the implementation available within ASE and after loosely interfacing with the LAMMPS³⁰ package. Atoms in the relaxed primitive cell of the Pd(110), Pd(100), and Pd(111) slabs are displaced by $\pm 10^{-3}$ Å along each of the x , y , and z directions. Laterally converged results for both the phonon band structures and spectral densities (as, e.g., those shown in Figs. 2–4 below) are obtained based on (6 × 6) multiples of the surface unit cell.

III. RESULTS AND DISCUSSION

A. Dissociative O₂ adsorption at low-index Pd surfaces

The dissociative adsorption of oxygen on the clean Pd(111), Pd(100), and Pd(110) surfaces is similarly exothermic, with PBE-DFT predicting the release of more than 2 eV per dissociating molecule. This similarity does not extend, however, to the underlying adsorption mechanism which varies between direct and/or precursor-mediated dissociation.^{35–38} Aiming here at a reliable representation of the O₂ bond scission as a starting point for the ensuing equilibration process, we focus on establishing in each case initial conditions of particular statistical relevance for the representative QM/Me-AIMD trajectories presented in the following. For modeling direct dissociation at Pd(100), we thus investigate the dominant entrance channel from the gas phase. To initialize trajectories in the precursor-mediated dissociation over Pd(110) and Pd(111),

FIG. 4. Same as Fig. 2 but for O₂ dissociating at Pd(111).

we focus instead on the more readily accessible transition states (TSs) between molecular and dissociative adsorption as identified via NEB calculations. A negligibly small initial kinetic energy is then properly distributed in the direction of the O_2 reaction coordinate simply to enforce the forward reaction which is subsequently dominated by the large intrinsic exothermicity of the dissociation event itself.

1. O_2 at Pd(100)

Classical MD simulations³⁹ performed on a DFT-based PES that has been interpolated within a neural-network approach⁴⁰ show direct dissociation at Pd(100) to proceed via one dominant entrance channel. This has gas-phase O_2 centering side-on above a fourfold hollow site with its molecular axis oriented along the [001] direction, i.e., in the direction of the neighboring hollow sites. The representative QM/Me-AIMD trajectory presented in the following is therefore initialized with molecular oxygen in such a configuration and at a height of 1.8 Å above the surface, where O–Pd energy exchange can still be considered negligible. The molecule is assigned an incident momentum normal to the surface that is consistent with the present PES description. Exploring the dominant entrance channel in nine further QM/Me-AIMD trajectories initialized at slightly different positions showed no qualitative effect on the central observables targeted here, i.e., the O–O end distances and concomitant phononic response.

2. O_2 at Pd(110)

A twofold adsorption mechanism is suggested on Pd(110) that exhibits a strong energy dependence and has precursor-mediated dissociation dominating in particular at low O_2 incident energies.³⁶ As we will describe in detail elsewhere,⁴¹ static DFT calculations exploring the high-symmetry adsorption sites on the relaxed, unreconstructed Pd(110) slab show molecular chemisorption to be preferred when O_2 lies parallel to the surface. Energetically favorable pathways underlying in fact both dissociation mechanisms are found to proceed via the fourfold hollow site and with the molecular axis oriented along the $[1\bar{1}0]$ direction, i.e., along the surface troughs. Investigating the low-coverage molecular precursor state in particular reveals a deep potential well ($E_b = 1.1$ eV) from which O_2 can escape via a low dissociation barrier ($E_{\text{diss}} = 173$ meV) that elongates the O–O bond and results in the adatoms separating along $[1\bar{1}0]$. The corresponding TS, combined with an initial O_2 kinetic energy of 25 meV, is used here as a starting point for the QM/Me-AIMD trajectory presented in the following. Qualitatively similar results are, however, also obtained for investigating diffusion along the [001] surface channels, i.e., by initializing O_2 from the less exothermic TS ($E_{\text{diss}} = 653$ meV) at a rotated top-hollow-top configuration (not shown). Nine trajectories in total overall confirm the qualitative picture discussed in the following regarding phononic dissipation and show no significant dependence on the initial kinetic energy or dissociative configuration.

3. O_2 at Pd(111)

Molecular beam experiments show no direct dissociation at Pd(111).^{37,38} The surface potential steers impinging O_2 instead into molecular precursor states from which thermally

accommodated oxygen can then only proceed to dissociation in a second step after sufficient heating. Here we predict the most stable such precursor states at the limit of low coverages as top-hollow-bridge configurations, i.e., with the O_2 center of mass essentially above a threefold hollow site and the molecular axis oriented along the $[1\bar{2}1]$ direction. Adsorption is energetically almost degenerate over the fcc and hcp hollow sites ($E_b = 891$ meV and 831 meV, respectively) and yields vibrational O–O stretching frequencies (903 cm^{-1} and 873 cm^{-1} , respectively) that are in good agreement with previous theoretical work.^{42,43} These values may equally well represent the frequency measured for the most abundant molecularly chemisorbed species at low coverages ($800\text{--}840\text{ cm}^{-1}$, depending on experimental conditions) by high-resolution electron energy loss spectroscopy (HREELS).⁴⁴ Consistently, both molecular configurations exhibit similarly high dissociation barriers ($E_{\text{diss}} = 686$ meV and 621 meV, respectively) along the calculated minimum energy paths that lead to a pair of oxygen atoms optimally adsorbed at identical neighboring hollow sites (hcp-hcp and fcc-fcc). Having no formal justification therefore for favoring either one or the other reaction path, we consider both involved TS geometries as the most probable candidate representatives for initializing nine O_2 /Pd(111) trajectories in total. These start from exploring the strict vicinity of the aforementioned TSs for molecular oxygen and differ slightly in the assigned initial kinetic energy (in the range of 5–50 meV). While the latter yield qualitatively similar results, the specific trajectory discussed in the following is initialized from the (exact) dissociative TS above hcp and with an O_2 kinetic energy of 25 meV.

B. Equilibration dynamics and “hot” adatoms

The top panels of Fig. 1 schematically illustrate the oxygen trajectories obtained following dissociation over Pd(110) (left), Pd(100) (middle), and Pd(111) (right), while d_{O-O} directly measures the adatom separation distance as a function of time. The evolution of kinetic energies in the lower panels shows how the released reaction energy initially accelerates the resulting O adatoms and decays thereafter into the Pd substrate. This decay clearly occurs on a picosecond time scale on all surfaces, i.e., it is not instantaneous on the time scale of the actual dissociation dynamics. An appreciable difference is, however, observed in the rate of energy transfer that decreases with increasing surface packing from Pd(110) over Pd(100) to Pd(111). This is most prominently reflected in the fraction of dissipated energy that has been propagated by phonons outside the QM embedding cells already on these time scales. Depicted by the shaded gray areas in Fig. 1, this amounts to 82%, 73%, and 54% of the total energy that has been dissipated to the substrate at ca. 1 ps after the initial O_2 bond dissociation over Pd(110), Pd(100), and Pd(111), respectively. This first quantitative estimate of heat transfer thus already underscores here the importance of augmenting self-standing AIMD simulations (that rely on, at most, several tens of substrate atoms) with a proper description of bulk dissipation and has important consequences for the actual adsorbate dynamics.

The varying dissipation rates on the three surfaces give rise to dissociation products of an intrinsically different degree of hyperthermal mobility. Efficient heat dissipation at Pd(110)

results in slow oxygen adatoms that are promptly captured by the surface potential at the immediately adjacent long-bridge sites. Figure 1 thus shows the adsorbates equilibrating at a distance of only one SLC (~ 2.8 Å) and already within a few tens of fs after the O₂ molecular bond breaks, i.e., even before they reach the (second nearest neighbor) quasi-threefold coordinated trough sites which are most favorable for atomic adsorption. This effectively lowers the amount of energy released during the ps-scale “hot” reaction to ca. 1.7 eV, as compared to the ideal 2.5 eV for adsorption over hollow. Dissociation over Pd(100) and Pd(111) results instead in translationally “hot” products whose transient mobility is marked by a series of hyperthermal diffusive hops (indicated by arrows in Fig. 1) between neighboring binding sites. A largely increasing separation distance d_{O-O} is found on Pd(100) as the adatoms follow a channel-type diffusive motion along the [001] direction. Two hyperthermal hops over bridge bring the adatoms to (the preferred Ref. 55) fcc hollow sites at four SLCs apart (~ 11.2 Å),⁴⁵ where they equilibrate within ca. 1 ps. A random-walk type diffusion is instead found on the densely packed Pd(111) surface which has the adatoms primarily trapped in the vicinity of hollow sites. Collisions with neighboring Pd atoms randomize the direction of the O lateral motion and the adatoms eventually occupy hcp hollow sites at a much smaller O–O separation distance of only two times the SLC (~ 5.6 Å). And yet, Fig. 1 reveals intriguingly hot adatoms on Pd(111) with significant fluctuations in kinetic energy even after the four barrier crossings counted along the presented 3 ps trajectory. In full agreement with experiment,⁸ similarly short end distances (in the range of 1-3 SLCs) are predicted by a total of nine QM/Me-AIMD trajectories, from which the extracted decay constants nevertheless suggest an average of 10 ps to a full thermalization.

Experimentally accessible product end distances can thus form a particularly misleading measure of adsorbate hyperthermal mobility.¹⁶ While not reflected here in the trend of equilibrium d_{O-O} values, transient hyperthermal lifetimes increase by approximately one order of magnitude for O₂ dissociating at each of the three low-index Pd surfaces. This is a particularly intriguing result given the similarly high exothermicity of the dissociative reactions (2.5, 2.3, and 2.7 eV at DFT-PBE level for the O adatoms optimally adsorbed at the favored hollow sites on Pd(110), Pd(100), and Pd(111), respectively) and barriers for atomic diffusion 421, 154, and 327 meV, respectively). The substantially different oxygen equilibration rates must therefore arise from qualitative differences in the underlying mechanism of phononic dissipation toward which we thus turn our attention in the following.

C. Exciting phonons

Based on the projection scheme laid out in Section II B, we analyze the corresponding phonon dynamics by evaluating the time-dependent (harmonic) phonon energies at specific time steps along the obtained QM/Me-AIMD trajectories. Even for the longest (3 ps) trajectories considered in this work, the total phononic energy $E_{\text{tot}}^{\text{ph}}$ calculated through Eq. (5) is found to be well contained within (40×40) repeating units of 40-layer surface primitive cells, i.e., well within the

boundaries of the employed MM region. In order to minimize the associated computational effort, commensurate reciprocal-space grids of a slightly reduced density are thus hereby employed to sample the corresponding twofold, fourfold, and sixfold two-dimensional surface Brillouin zones of the Pd(110), Pd(100), and Pd(111) substrates, respectively. Comparing to the equivalent $E_{\text{tot}}^{\text{ph}}$ representation obtained by directly evaluating the anharmonic MEAM potential then provides a measure for the total error introduced by projecting onto a harmonic solid. The latter is found in all cases to yield an additive offset contribution which is particularly small during the early stages of the dissipation dynamics. For the results presented in the following, we specifically calculate a negligibly small absolute error of <15 meV which thus conveys confidence in the emerging mechanistic analysis.

Energy resolved excitation spectra are calculated “on the fly” through a straightforward discretization of Eq. (4) along the energy ($\hbar\omega$) axis. While this greatly simplifies visualization, it is still the mode selectivity naturally provided by the underlying formalism that allows to focus on certain groups of modes. In particular the surface phonons obviously form a very prominent group in this context and are classified here as modes whose displacement eigenvector is localized to at least 20% in the two outermost slab layers. We verify that modifying this criterion has no qualitative effect on the presented results but yields only quantitative changes simply because more or less phonons are identified as surface modes.

Figures 2–4 show such excitation spectra calculated at $t = 50$ fs along the presented QM/Me-AIMD trajectories, i.e., during the very early stages of the oxygen adsorption dynamics. Intriguingly, despite their negligible spectral weight illustrated by the phononic density of states (DOS) in the middle panels, surface modes are found in all cases to carry a substantial fraction (45%, 45%, and 33% for Pd(110), Pd(100), and Pd(111), respectively) of the total energy that has been dissipated into the substrate at that time. Qualitative differences, however, in the phononic response have already set in and are clearly apparent.

At Pd(110) the dissipated energy is distributed within the entire frequency range of the phonon band structure which is given for reference in the leftmost panel of Fig. 2. The latter is decorated by a rich spectrum of both pure and resonant surface states (outlined by black markers), as expected by the large structural relaxation at this open surface.³² The rightmost panel of Fig. 2 shows a strong non-equilibrium population of these modes (in black), with a significant fraction (33%) of the surface energy lying within a bulk-hybridized resonant state at intermediate frequencies (13-15 meV) that displays a predominantly longitudinal displacement pattern as it (partially) extends along $\bar{\Gamma}-\bar{Y}$ (confirmed also in previous theoretical studies^{32,46}). Quite in contrast therefore to what is predominantly assumed about energy sinks in model bath Hamiltonians (cf., for example, see Ref. 47 and references therein), it is not the Rayleigh modes here that become dominantly excited although lying energetically below the onset of the bulk part of the spectrum. Anharmonic decay of the different Pd(110) surface excitations overall leads, already at this time, to substantial bulk excitation that obviously does not (directly) result from interaction with the adsorbate alone.

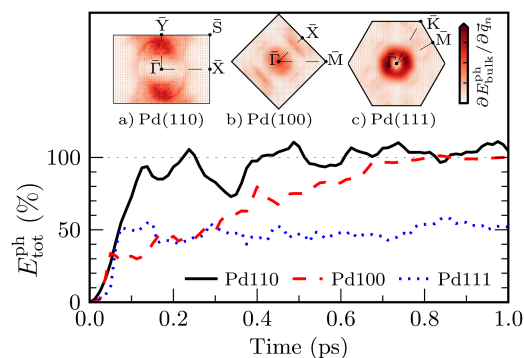


FIG. 5. Phononic energy uptake along the presented QM/Me-AIMD trajectories as a fraction of the theoretically predicted chemical energy released during the “hot” reaction of O_2 dissociation at Pd(110) (solid black line), Pd(100) (dashed red line), and Pd(111) (dotted blue line). Insets (a, b, c): Distribution of bulk Pd kinetic energy over the two-dimensional surface Brillouin zones of the three surfaces at $t = 100$ fs. The coloring is based on a linear interpolation between values at exact phonon wavevectors (\vec{q}_n , black markers) at which the kinetic energy of all bulk phonon branches has been summed.

Visualizing the distribution of bulk kinetic energy over the two-dimensional Pd(110) Brillouin zone at $t = 100$ fs (cf. inset of Fig. 5) reveals indeed a strongly perturbed phononic system with excitations spreading primarily around the \bar{Y} symmetry point.

Figure 3 shows a qualitatively different picture at Pd(100) where the dissipated energy is highly concentrated in a single surface optical band of high frequencies (21-22 meV) that lies in a pseudogap between the bulk modes, in accordance with Refs. 16 and 24. Analyzing the mode eigenvectors straightforwardly rationalizes this unexpected non-Rayleigh excitation^{16,24} by the preferred binding site of the O adatoms. Rather than indenting the topmost substrate layer upon impingement, which is the picture suggesting a predominant excitation of corresponding Rayleigh modes, the dissociating O atoms penetrate directly into the hollow sites and subsequently diffuse laterally over bridge sites along one of the [001] surface channels. Along this motion they rather push the top-layer Pd atoms laterally away, which corresponds exactly to the purely longitudinal displacement pattern of the modes belonging to the aforementioned surface optical phonon band.^{32,46}

The random-walk type diffusion of oxygen on Pd(111) leads instead to a weighted phonon population that essentially follows the surface DOS, cf. Fig. 4. Similar to Pd(100), high-frequency optical modes with a longitudinal character promptly decay into large wavelength bulk modes that reside in the strict vicinity of the $\bar{\Gamma}$ -point, cf. insets of Fig. 5. The larger fraction of the released chemical energy is, however, contained within low-frequency acoustic phonons at short wavelengths. With their small group velocities, these notoriously long-lived Rayleigh waves⁴⁸ efficiently confine the released energy at the surface and within a small reaction zone around the O_2 impingement region. Within this region, anharmonic phonon-phonon interactions quickly establish a quasi-equilibrium state that is sufficiently well described by a Planckian distribution. An effective local temperature extracted therefrom shows an increasingly “hot” surface that contrasts the corresponding bulk behavior and confirms minimal coupling between the two phononic sub-systems over the entire course of the QM/Me-AIMD trajectory.¹⁶

The substantially different equilibration rates on the three surfaces are thus ultimately determined by microscopic details of the interfacial energy exchange. Efficient heat dissipation at Pd(110) is channeled through the multitude of surface excitations at a constant rate of ~ 10 meV/fs, as extracted from the evolution of the total phonon energy ($E_{\text{tot}}^{\text{ph}}$) in Fig. 5. The vast majority (94%) of the theoretically predicted 1.7 eV is thus already dissipated within the first 150 fs of the adsorption dynamics (while subsequent fluctuations around 100% reflect oxygen’s metastable adsorption at the long-bridge sites). This contrasts the corresponding value of 0.79 eV for Pd(100) at this time. Nevertheless, a largely increasing phononic energy uptake is also observed here through the (sub-ps) anharmonic decay of the aforementioned highly populated surface optical band. Saturation of $E_{\text{tot}}^{\text{ph}}$ (at the theoretical value of 2.3 eV) is thus reached within about 1 ps after the initial O_2 bond dissociation and at a concomitant longer lifetime of the hyperthermal state. The substantially slower equilibration at Pd(111) results instead from the dominant excitation of long-lived Rayleigh waves which spatially confine the released chemical energy. As reflected by the non-monotonic behavior in the total phononic energy uptake, this promotes a back and forth O–Pd energy exchange and rationalizes the exceptional hyperthermal mobility observed at this surface.

The presented analysis thus offers a first-principles perspective on parameters entering effective models of substrate mobility, such as the prevalent Surface Oscillator⁴⁹ (SO) and Generalized Langevin Oscillator^{11–13} (GLO) methodologies. Our results show that phononic excitations are intrinsically more complicated than postulated in common-practice representations of a single (usually low-frequency) surface oscillation⁵⁰ and certainly not transferable even between different surfaces of the (chemically) same substrate. As heralded however by recent first-principles based SO/GLO applications of H_2 at Pd,⁵¹ investigated statistical properties (typically sticking or scattering probabilities) have so far demonstrated an exceptional insensitivity with respect to such input frequency parameters.

With increasing reaction exothermicity and/or concomitant adsorbate-substrate vibrational coupling, a higher sensitivity to the underlying phononic fine structure might nevertheless still be expected. Occurrences of resonant phenomena involving selective-phonon excitations are indeed not unheard of and have, for example, been shown to play an important role in the sticking of light H_2 , HD molecules at metal surfaces.¹⁴ We observe here a similar effect for O_2 dissociation and subsequent channel-type diffusion at Pd(110) and Pd(100) which, however, does not involve the predominantly assumed Rayleigh excitation but rather optical surface modes at higher frequencies. The “right” surface excitations can thereby only be extracted from a detailed microscopic phonon analysis such as the one presented here. Picking up on these frequencies to use as input parameters in more numerically efficient heat bath models is now an obvious step forward. Whether the approximate nature of the latter will, however, allow for lifting the aforementioned insensitivity and capturing selective-adsorption resonances remains yet open to investigation.

IV. SUMMARY AND CONCLUSIONS

In summary, we augmented *ab initio* molecular dynamics simulations with a quantitative account of phononic dissipation and studied the equilibration process ensuing the exothermic oxygen dissociation at all low-index (110), (100), and (111) Pd surfaces. The specific motivation was to elucidate the influence of substrate symmetry on the resulting hyperthermal adatom mobility, while assessing the level of detail required to be accounted for in the underlying phonon excitations. We observe a striking difference in the hot O lifetime that decreases from Pd(110) over Pd(100) to Pd(111) and is not overall reflected in experimentally accessible product end distances. Whilst difficult to reconcile on purely energetic grounds, this finding already demonstrates a complex dependence on microscopic details of the dissipative dynamics.

Relying on our atomically resolved description of a macroscopic heat bath, we unravel mechanistic details of the energy conversion process through a mode-specific phonon analysis. This reveals qualitative differences in the phononic response setting in already during the very first steps of oxygen dissociation. Excitation of specific groups of localized surface modes sets the initial conditions for the ensuing phonon relaxation which is manifested through anharmonic phonon-phonon interactions and leads to intrinsically different rates of dissipation to the Pd bulk. Demonstrating how critically these microscopic details may influence the actual adsorbate dynamics thus nicely highlights the strengths of QM/Me embedding compared to previous theoretical treatments of phononic dissipation. Wahnström and co-workers, for example, entirely neglected such early surface excitations due to limitations of their semi-empirical potential in describing O₂ dissociation at Al(111) and concluded on minimal adsorbate-phonon coupling.⁵² On the other hand, stand-alone AIMD simulations provide the desired predictive-quality chemical description but will unavoidably falsify the demonstrated picosecond-scale adsorbate equilibration due to the finite extent of computationally tractable supercells.¹⁵

With qualitatively different surface excitations observed at both the high- and low-frequency regimes, we illustrate from a first-principles perspective a complex multi-phonon picture for the non-equilibrium adsorbate-phonon dynamics such as the one suggested in early experimental work for NO at Ag(111), for example.⁵³ In the meantime, we highlight the danger of generalizing the single-phonon approximation to strongly chemisorbing adsorbates that go beyond prototypical studies of light atom/molecule scattering.⁵⁴ In a systematic comparison with respect to surface symmetry, we relate real-space trajectories to the specific oxygen-induced excitations which can be subsequently used as input parameters for computationally attractive models of an effective substrate mobility.

ACKNOWLEDGMENTS

S. P. Rittmeyer is thanked for many stimulating discussions. Funding through the Deutsche Forschungsgemeinschaft is acknowledged within Project No. RE1509/19-1, as is generous access to CPU time through the Leibniz Rechenzentrum

der Bayerischen Akademie der Wissenschaften (Project No. pr85wa).

- ¹J. Barth, *Surf. Sci. Rep.* **40**, 75 (2000).
- ²L. C. Ciacchi and M. C. Payne, *Phys. Rev. Lett.* **92**, 176104 (2004).
- ³A. Carley, P. Davies, and M. Roberts, *Catal. Lett.* **80**, 25 (2002).
- ⁴H. Brune, J. Wintterlin, R. J. Behm, and G. Ertl, *Phys. Rev. Lett.* **68**, 624 (1992).
- ⁵S. Schintke, S. Messerli, K. Morgenstern, J. Nieminen, and W.-D. Schneider, *J. Chem. Phys.* **114**, 4206 (2001).
- ⁶M.-F. Hsieh, D.-S. Lin, H. Gawronski, and K. Morgenstern, *J. Chem. Phys.* **131**, 174709 (2009).
- ⁷C. Sprokowski, M. Mehlhorn, and K. Morgenstern, *J. Phys.: Condens. Matter* **22**, 264005 (2010).
- ⁸M. Rose, A. Borg, J. Dunphy, T. Mitsui, D. Ogletree, and M. Salmeron, *Surf. Sci.* **561**, 69 (2004).
- ⁹J. Wintterlin, R. Schuster, and G. Ertl, *Phys. Rev. Lett.* **77**, 123 (1996).
- ¹⁰M. Schmid, G. Leonardelli, R. Tschelieng, A. Biedermann, and P. Varga, *Surf. Sci.* **478**, L355 (2001); A. J. Komrowski, J. Z. Sexton, A. C. Kummel, M. Binetti, O. Weiße, and E. Hasselbrink, *Phys. Rev. Lett.* **87**, 246103 (2001).
- ¹¹S. A. Adelman and J. D. Doll, *J. Chem. Phys.* **64**, 2375 (1976).
- ¹²J. C. Tully, *J. Chem. Phys.* **73**, 6333 (1980).
- ¹³J. C. Polanyi and R. J. Wolf, *J. Chem. Phys.* **82**, 1555 (1985).
- ¹⁴M. D. Stiles and J. W. Wilkins, *Phys. Rev. Lett.* **54**, 595 (1985).
- ¹⁵J. Meyer and K. Reuter, *Angew. Chem., Int. Ed.* **53**, 4721 (2014).
- ¹⁶V. J. Bukas and K. Reuter, *Phys. Rev. Lett.* **117**, 146101 (2016).
- ¹⁷H. Lin and D. Truhlar, *Theor. Chem. Acc.* **117**, 185 (2007).
- ¹⁸C. Bo and F. Maseras, *Dalton Trans.* **2008**, 2911.
- ¹⁹N. Bernstein, J. R. Kermode, and G. Csányi, *Rep. Prog. Phys.* **72**, 026501 (2009).
- ²⁰M. M. Siddick, G. J. Ackland, and C. A. Morrison, *J. Chem. Phys.* **125**, 064707 (2006).
- ²¹N. de Koker, *Phys. Rev. Lett.* **103**, 125902 (2009).
- ²²N. de Koker, *Earth Planet. Sci. Lett.* **292**, 392 (2010).
- ²³A. J. H. McGaughey and M. Kaviani, *Phys. Rev. B* **69**, 094303 (2004).
- ²⁴J. Meyer, "Ab initio modeling of energy dissipation during chemical reactions at transition metal surfaces," Ph.D. thesis, Freie Universität Berlin, Germany, 2012.
- ²⁵J. P. Perdew, K. Burke, and M. Ernzerhof, *Phys. Rev. Lett.* **77**, 3865 (1996); **78**, 1396 (1997).
- ²⁶S. S. Alexandre, E. Anglada, J. M. Soler, and F. Yndurain, *Phys. Rev. B* **74**, 054405 (2006); D. A. Stewart, *New J. Phys.* **10**, 043025 (2008).
- ²⁷C. Carbogno, A. Gross, J. Meyer, and K. Reuter, in *Dynamics of Gas-Surface Interactions*, Springer Series in Surface Sciences, Vol. 50, edited by R. D. Muiño and H. F. Busnengo (Springer, 2013), pp. 389–419.
- ²⁸V. Blum, R. Gehrke, F. Hanke, P. Havu, V. Havu, X. Ren, K. Reuter, and M. Scheffler, *Comput. Phys. Commun.* **180**, 2175 (2009).
- ²⁹H. J. Monkhorst and J. D. Pack, *Phys. Rev. B* **13**, 5188 (1976).
- ³⁰S. Plimpton, *J. Chem. Phys.* **117**, 1 (1995).
- ³¹M. I. Baskes, *Phys. Rev. B* **46**, 2727 (1992).
- ³²R. Heid and K.-P. Bohnen, *Phys. Rep.* **387**, 151 (2003).
- ³³S. R. Bahn and K. W. Jacobsen, *Comput. Sci. Eng.* **4**, 56 (2002).
- ³⁴G. Henkelman, B. P. Uberuaga, and H. Jansson, *J. Chem. Phys.* **113**, 9901 (2000).
- ³⁵A. den Dunnen, S. Wiegman, L. Jacobse, and L. B. F. Juurlink, *J. Chem. Phys.* **142**, 214708 (2015).
- ³⁶P. Junell, K. Honkala, M. Hirsimäki, M. Valden, and K. Laasonen, *Surf. Sci.* **546**, L797 (2003).
- ³⁷P. Sjövall and P. Uvdal, *Chem. Phys. Lett.* **282**, 355 (1998).
- ³⁸P. Nolan, B. Lutz, P. Tanaka, and C. Mullins, *Surf. Sci.* **419**, L107 (1998).
- ³⁹V. J. Bukas, S. Mitra, J. Meyer, and K. Reuter, *J. Chem. Phys.* **143**, 034705 (2015).
- ⁴⁰V. J. Bukas, J. Meyer, M. Alducin, and K. Reuter, *Z. Phys. Chem.* **227**, 1523 (2013).
- ⁴¹V. J. Bukas and K. Reuter, "A comparative study of atomic oxygen adsorption at Pd surfaces from Density Functional Theory" (unpublished).
- ⁴²A. Eichler, F. Mittendorfer, and J. Hafner, *Phys. Rev. B* **62**, 4744 (2000).
- ⁴³K. Honkala and K. Laasonen, *J. Chem. Phys.* **115**, 2297 (2001).
- ⁴⁴K. W. Kolasinski, F. Cemic, and E. Hasselbrink, *Chem. Phys. Lett.* **219**, 113 (1994).
- ⁴⁵We ensure the equilibrium end-distance is not limited by unphysical O–O interactions through lateral periodic images of the embedding cell by pausing the QM/Me trajectory at a point for which $d_{O-O} = 3$ SLCs,

i.e., where substrate mediated adsorbate interactions are expected to have largely vanished.⁵⁵ We thereby continue integration based on *two* (3×3) QM embedding cells centered around each oxygen atom and treated independently on the DFT level (yet still coupled via the substrate motion described on the MEAM level). Having the cells dynamically “follow” the motion of the individual oxygen atoms over the surface reproduces the original trajectory, thus conveying further trust in both the embedding approach and the resulting maximum adatom separation distance.

⁴⁶I. Sklyadneva, G. Rusina, and E. Chulkov, *Surf. Sci.* **377**, 313 (1997).

⁴⁷M. D. Stiles, J. W. Wilkins, and M. Persson, *Phys. Rev. B* **34**, 4490 (1986); B. Jackson, *Comput. Phys. Commun.* **63**, 154 (1991); **80**, 119 (1994); *J. Chem. Phys.* **108**, 1131 (1998).

⁴⁸S.-I. Tamura, *Phys. Rev. B* **30**, 610 (1984).

⁴⁹M. Hand and J. Harris, *J. Chem. Phys.* **92**, 7610 (1990).

⁵⁰G.-J. Kroes, *Science* **321**, 794 (2008).

⁵¹H. F. Busnengo, W. Dong, P. Sautet, and A. Salin, *Phys. Rev. Lett.* **87**, 127601 (2001); H. F. Busnengo, W. Dong, and A. Salin, *ibid.* **93**, 236103 (2004); H. F. Busnengo, M. A. Di Césare, W. Dong, and A. Salin, *Phys. Rev. B* **72**, 125411 (2005).

⁵²C. Engdahl and G. Wahnström, *Surf. Sci.* **312**, 429 (1994); G. Wahnström, A. B. Lee, and J. Strömquist, *J. Chem. Phys.* **105**, 326 (1996).

⁵³D. J. Auerbach, *Phys. Scr.* **1983**, 122.

⁵⁴A. S. Sanz and S. Miret-Artés, *Phys. Rep.* **451**, 37 (2007).

⁵⁵Y. Zhang, V. Blum, and K. Reuter, *Phys. Rev. B* **75**, 235406 (2007).